Title
Characterization of the Thermal Properties of Ir/Pt Bilayer Transition Edge Sensors

Journal
Journal of Low Temperature Physics, 210(1-2)

ISSN
0022-2291

Authors
Zhang, J
Chang, CL
Fujikawa, B
et al.

Publication Date
2023

DOI
10.1007/s10909-022-02811-y

Peer reviewed

Noname manuscript No.
(will be inserted by the editor)

Characterization of the Thermal Properties of Ir/Pt Bilayer Transition Edge Sensors

J. Zhang · C. L. Chang · B. Fujikawa · G. Karapetrov · Yu. G. Kolomensky · W.-K. Kwok · M. Lisovenko · V. Novosad · J. Pearson · V. Singh · G. Wang · B. Welliver · U. Welp · V. G. Yefremenko

Received: date / Accepted: date

Abstract We are developing a low-T_c-TES based large area and low threshold detector targeting a variety of potential applications. The detector consists of a 50.8 mm diameter Si wafer as the substrate and radiation absorber, a single Ir/Pt bilayer TES sensor in the center, and normal metal Au pads added to the TES to strengthen the TES-absorber thermal coupling. Tight TES-absorber thermal coupling improves detector sensitivity and response uniformity. Here we report on the electron-phonon (e-ph) coupling strengths for the Ir/Pt bilayer and Au that are measured with our prototype detectors and TES devices. We found that a second weak thermal link besides the one due to e-ph coupling in Ir/Pt or Au was required to explain our data. With the effects of the second weak link accounted for, the extracted e-ph coupling constant Σ for Ir/Pt bilayer in the T_c range between 32 mK and 70 mK is 1.9×10^8 WK^{-5}m^{-3}, and Σ's for Au at 40 mK and 55 mK are 2.2×10^9 WK^{-5}m^{-3} and 3.2×10^9 WK^{-5}m^{-3}, respectively.

Keywords transition edge sensor · electron-phonon coupling · iridium platinum bilayer · gold

J. Zhang · C. L. Chang · M. Lisovenko · G. Wang · V. G. Yefremenko
High Energy Physics Division, Argonne National Laboratory, Lemont, IL 60439, USA
E-mail: jianjie.zhang@anl.gov

W.-K. Kwok · V. Novosad · J. E. Pearson · U. Welp
Materials Science Division, Argonne National Laboratory, Lemont, IL 60439, USA

C. L. Chang
Kavli Institute for Cosmological Physics and the Department of Astronomy and Astrophysics, University of Chicago, Chicago, IL 60637, USA

Yu. G. Kolomensky · V. Singh · B. Welliver
Department of Physics, University of California, Berkeley, CA 94720, USA

B. Fujikawa · Yu. G. Kolomensky · B. Welliver
Nuclear Science Division, Lawrence Berkeley National Laboratory, Berkeley, CA 94720, USA

G. Karapetrov
Physics Department, Drexel University, Philadelphia, PA 19104, USA

1 Introduction

We are developing an Ir/Pt-bilayer-TES based large area and low threshold detector targeting a variety of potential applications, such as direct detection of low-mass Dark Matter (DM), Coherent Elastic Neutrino Nucleus Scattering (CEvNS), cryogenic search of Neutrinoless Double Beta Decay ($0\nu\beta\beta$), and high precision spectroscopy. For low-mass DM detection, the detector threshold determines the lowest DM mass detectable by an experiment. The CEvNS process through neutral current interaction is thresholdless, i.e., the lower the detector threshold gets, the higher the fraction of neutrinos can be detected, resulting in improved experimental sensitivity. This is especially true for reactor neutrino sources. One particularly well motivated application is the CUPID (CUORE Upgrade with Particle IDentification) experiment [1], the next-generation bolometric search for $0\nu\beta\beta$, where the detector is used as a light detector (LD) to detect the Cerenkov or scintillation light generated in the bolometer crystal. The detected light signal, together with the heat signal from the bolometer, is used to reject background events. Other than background rejection, the light signal can potentially extend the science reach of the experiment [1].

As given by the TES physics, the detector baseline resolution $\Delta E_{\mathrm{FWHM}} \propto \sqrt{4k_{\mathrm{B}}T_0^2C}$ [2], where k_{B} is the Boltzmann constant, T_0 is the TES electron temperature which can be taken as the TES superconducting transition temperature T_c, and C is the detector heat capacity. The lowest detector threshold is only achievable at the lowest TES operating temperature, which is our ultimate goal. This paper presents results for T_c 40-60mK, which would give sufficiently low thresholds for applications like CUPID. We will eventually lower the T_c of the detector down to sub-20 mK based on our R&D work at elevated T_c's.

The prototype LDs we are developing consist of a square Ir/Pt bilayer TES, a 50.8 mm diameter and 275 μm thick high resistivity Si wafer as the substrate and light absorber, and superconducting Nb electrical leads. The square TES is patterned in the center of the Si wafer to maximize its response uniformity. The LD is intended to be a thermal detector, for which the TES sensor response will be optimized to the overall temperature change of the light absorber, and as such, the event position dependence is maximally reduced. The primary thermal conductance, G, for the LD is between the Si absorber and the thermal bath, which determines the time constant of the LD as $\tau \propto C/G$. The TES sensor and the absorber are thermally tightly coupled such that the temperature swing of both are nearly synchronized during an event. So it is necessary to substantially strengthen the thermal coupling between the Ir/Pt TES and the Si absorber beyond the e-ph coupling of the Ir/Pt bilayer. Normal metal Au is added to the TES for this purpose. In this paper, we report on the e-ph coupling strengths for Ir/Pt bilayer and Au that are measured with our prototype LDs and TES devices. These results serve as the basis for our future LD design and optimization.

2 Device Description

We have fabricated and measured two types of TES devices. One consists of only a square Ir/Pt bilayer TES as shown in Fig. 1(a), and the other consists of a square Ir/Pt bilayer TES and a pair of Au pads symmetrically patterned over the TES edges as shown in Fig. 1(b). The second type of devices behave similarly as a single superconducting TES, with enhanced thermal coupling to the substrate from the added normal metal pads. We therefore call both types of devices as TES and refer to the former as bare TES if distinction between the two is needed.

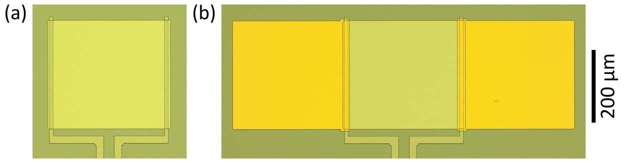

Fig. 1: Example micrographs of the TES devices in this work: (a) a square Ir/Pt bilayer TES and (b) a square Ir/Pt bilayer TES in the middle with a pair of Au pads. Nb leads are deposited over the edges of the TESs for both layouts. The sizes of both the Ir/Pt bilayers and Au pads for the devices shown are 300 μm $\times$ 300 μm.

Fabrication of the TESs was carried out at the Argonne National Laboratory. All the TESs in this work were fabricated on high resistivity Si substrates with a nominal thickness 275 μm. The TESs were patterned with photolithography and the films were sputtering deposited at room temperature in the order of Ir/Pt bilayer, Au pads, and Nb leads. The Ir layer thickness was kept at 100 nm, whereas the thickness of the Pt layer was varied to tune the T_c of the bilayer via proximity effect. The T_c range around 40-60 mK was found to allow adequate LD performance based on our simulations, and the thicknesses of the Pt layer were chosen accordingly. The deposition order of Ir and Pt for the bilayer did not affect its T_c or transition profile for the test samples we measured. Au pads of 200 nm thick were deposited after the Ir/Pt bilayer, each forming a 15-20 μm wide overlap region with the latter along the edge. A thin Ir layer around 3 nm was deposited underneath the Au layer to increase the adhesion to the Si substrate. Nb leads with thickness 200 nm were deposited over the overlap regions of the Ir/Pt bilayer and Au, which were terminated near the edge of the Si substrate as a pair of wirebond pads. The film thickness uncertainties of the sputtering process were less than 3% [3].

The layout configurations of the TESs in this work are summarized in Tables 1 and 2. All the devices were first fabricated on ⌀50.8 mm Si wafers, and then diced into cm-sized chips for measurement, except TP-1, IrPt-S005, and IrPt-S006 which were prototype LDs. The devices TP-1, JT-1, and JT-2 used a different Ir target from the rest of the TESs, and the deposition conditions were different between TP-1 and JT-x, making direct T_c comparison infeasible if either difference is involved. However, since the T_c's of these three devices are about in the same range as those for the rest, we still include them in reporting the e-ph coupling constants for the It/Pt bilayers.

3 Experimental Setup and Measurements

We measured all the TESs in this work inside a Bluefors LD400 Dilution Refrigerator (DR) with a base temperature below 7 mK. To measure the e-ph coupling strength of Ir/Pt and Au, the substrates of the devices were thermally grounded to the thermal bath. The TES chips were glued directly to a Cu sample holder with a thin layer of rubber cement. The prototype LDs were clamped down to a Cu wafer holder by four PELCO SEMClip$^{\mathrm{TM}}$ clips near the wafer edge. A thin layer of Apiezon N grease was applied between the wafer and the holder to ensure good thermal contact. The wafer holder has a 44.4 mm diameter hole in the center to avoid overly stressing the wafer. The TESs were electrically connected to the bias circuit via Al wire bonds with T_c around 1 K. The total parasitic resistance introduced in the TES wiring was typically 4 mΩ, whose effect is negligible for our TESs with R_n

Table 1: TES layout information and measured thermal properties for the bare Ir/Pt TESs. The Ir layer is 100 nm thick. The Pt layer thicknesses and the TES sizes are listed in the table. The parameters T_c, G, and Σ are from the fits to the power law in Eq. (1) with $n = 5$.

Device	Pt (nm)	TES (μm)	T_c (mK)	P_{sat} (pW)	G (nW/K)	Σ ($WK^{-5}m^{-3}$)
TP-1	20[1]	500	41.0	0.89	0.11	2.5×10^8
JT-1	40[1]	500	60.0	4.50	0.38	1.7×10^8
JT-2	80[1]	500	32.5	0.35	0.053	2.1×10^8
IrPt-S005	60	500	43.7	1.35	0.15	2.1×10^8
IrPt-S006	40	100	69.8	0.56	0.040	2.4×10^8
MC-12-1	50	300	58.5	1.46	0.12	1.6×10^8
MCC-4-1	60	100	36.7	0.028	0.0039	2.7×10^8
MCC-4-2	60	200	39.8	0.11	0.014	1.8×10^8
MCC-4-3	60	300	41.3	0.26	0.031	1.5×10^8
MCC-4-4	60	400	42.2	0.43	0.050	1.2×10^8

[1] The 100 nm thick Ir layer was deposited before the Pt layer for these devices.

around 0.5 Ω. The assembled TES modules were mounted onto the mixing chamber stage of the DR. Two ruthenium oxide thermometers were installed to monitor the temperatures of the TES device holder and the mixing chamber plate. The temperature readings were cross checked to ensure consistency. The RMS uncertainties on temperature readings were typically within 0.1 mK.

The TESs were voltage biased with 17.6 mΩ shunt resistors. TES current for each device was read out by an inductively coupled two-stage phase-locked DC SQUID amplifier from STAR Cryoelectronics. We took IV and RT measurements for all the devices. IV curves were taken by sweeping the DC bias voltage of the TES from the normal state to zero bias. At each voltage set point, the sweep paused for 1 s for the TES to reestablish equilibrium, which was long enough for the TESs in this work. A series of IV curves, each at a different bath temperature, were taken for each TES. The RT curves for the TESs were taken with a low frequency (<20 Hz) small AC bias ($I_{bias} = 0.3$–$1\ \mu A$) to check the T_c independently.

4 Data Analysis

4.1 Analysis method

The dominant cooling mechanism for these TESs when biased in superconducting-to-normal transition is expected to be electron-phonon coupling of the form

$$P = \Sigma \Omega (T^n - T_b^n), \tag{1}$$

where P is the TES Joule heating power, Σ is the e-ph coupling constant, Ω is the TES volume, T is the TES electron temperature, T_b is the thermal bath temperature, and the exponent n is usually between 5 and 6 [4,5,6]. Our TES devices operated in the strong electrothermal feedback regime, where the TES electron temperature T was very close to the transition temperature T_c. We therefore did not distinguish them in our analysis.

The usual approach to analyze the P-T curve shown in Fig. 3(b) is to fit the measured data to the single-block power law of Eq. (1), the result of which is shown as the orange dash-dotted line with the fitted $n = 4.6$. It is not uncommon, for the bare Ir/Pt TES devices we have measured, that the fitted exponent n from the single-block model is slightly lower or higher than the characteristic value 5 for e-ph coupling. The small deviations of n, however, would cause large variations on the parameter Σ, which we were trying to measure. We carefully examined the potential sources of the systematics of our measurements, including the uncertainties on the bias and output voltages, bath temperature readings, and hypothesized external thermal loads on the TES; and none of these is large enough to account for our observation. This leads to the conclusion that the one-block model is not adequate to describe the behavior of the bare Ir/Pt devices. We therefore introduced the two-block thermal model shown in Fig. 2(a). As it turned out, a different form of the two-block model as depicted in Fig. 2(b) is required to describe the TESs with Au pads. We leave the application details of the two-block model to the specific type of devices to the sections below, and discuss the general picture in this section.

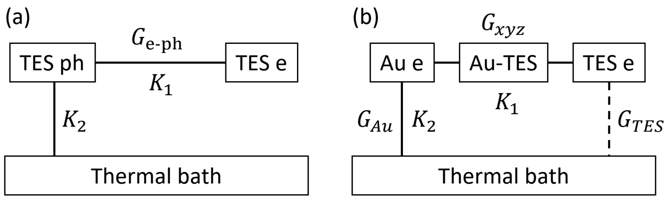

Fig. 2: (a) Two-block model for bare Ir/Pt TES. (b) Two-block model for TES with Au pads.

As shown in Fig. 2, the two-block model has two thermal impedances, K_1 and K_2, connected in series between the electrons of TES and the thermal bath. The power flows across the two thermal impedances each is assumed to follow a power law in the form of Eq. (1). Thermal power flow balance gives

$$P = K_1(T^h - T_a^h) = K_2(T_a^m - T_b^m) \equiv K(T^n - T_b^n), \tag{2}$$

where T_a is the temperature of an intermediate stage, i.e., TES phonons in Fig. 2(a) or Au electrons in Fig. 2(b), h and m are the exponents of the power laws for K_1 and K_2, respectively, and the overall behavior of the device is still given by Eq. (1). The specific form of K_1 or K_2 depends on the mechanism of the heat conduction, and for e-ph coupling, it is given by $\Sigma\Omega$, the product of e-ph coupling constant and the volume.

A two-block fitting method can be constructed from the above model. For a set of measurements of the bath temperature and the TES Joule power, $(T_{bi},\ P_i)$, $i = 1,\ldots,N$, the χ^2 of the fit can be defined as

$$\chi^2 = \sum_{i=1}^{N} \frac{(P_i - K_2(T_{ai}^m - T_{bi}^m))^2}{\sigma_{P_i}^2}, \tag{3}$$

where T_{ai} is the solution to the equation

$$K_1(T^h - T_{ai}^h) = K_2(T_{ai}^m - T_{bi}^m), \tag{4}$$

and σ_{P_i} is the standard deviation of P_i. The value of σ_{P_i} can in principle be estimated from the measurements, however, we have simply taken it as unity in our analysis because σ_{P_i}'s are small and their contribution to the the uncertainties of Σ is insignificant. The uncertainties of T_{bi} are also neglected for the same reason. At the end, we have arrived at a nonlinear least-squares fitting method with T, K_1, K_2, h, and m as the fitting parameters. Because of the degeneracy in parameter space, it is generally desirable to fix some parameters that can be determined through other means or known as priors when applying this method.

Thermal conductance is an important quantity for the TES device. Assuming the thermal bath is at a constant temperature, for the single-block model, the thermal conductance G is given by

$$G = \frac{\mathrm{d}P}{\mathrm{d}T} = nKT^{n-1}. \tag{5}$$

The thermal conductances for impedance blocks K_1 and K_2 can be defined similarly,

$$G_1 = \frac{\partial P}{\partial T} = hK_1T^{h-1}, \tag{6}$$

$$G_2 = \frac{\partial P}{\partial T_a} = mK_2T_a^{m-1}. \tag{7}$$

The total thermal conductances for the two-block model, defined with respect to K_1 and K_2 are given by

$$G = \left(\frac{\mathrm{d}P}{\mathrm{d}T}\right)_{K_1} = hK_1T^{h-1} - hK_1T_a^{h-1}\frac{\mathrm{d}T_a}{\mathrm{d}T}, \tag{8}$$

$$G = \left(\frac{\mathrm{d}P}{\mathrm{d}T}\right)_{K_2} = mK_2T_a^{m-1}\frac{\mathrm{d}T_a}{\mathrm{d}T}. \tag{9}$$

Combining Eqs. (6), (7), (8), and (9), we obtain

$$G = \frac{G_1G_2}{G_1(T_a/T)^{h-1} + G_2}. \tag{10}$$

When the bath temperature is close to the superconducting transition temperature, T_a/T approaches unity and we recover the expression for linear thermal conductances connected in series.

4.2 Σ for Ir/Pt bilayer

The first goal of this work is to measure the e-ph coupling constant Σ of the Ir/Pt bilayers. Fig. 3(a) shows the measured IV curves for the TES device MCC-4-3 at a series of bath temperatures. At a given bath temperature, the Joule power of a TES within the superconducting-to-normal transition is largely a constant due to strong negative electrothermal feedback. This is especially true for the bare Ir/Pt TESs whose saturation powers are small. We plot the Joule power of the TES at a fixed TES resistance close to R_n against the bath temperature as the black circles in Fig. 3(b). The green dashed line in the same plot shows the fit to the power law in Eq. (1) with $n = 5$. The thermal parameters extracted from the fit are the transition temperature $T_c = 41.3$ mK, the thermal conductance $G = 0.031$ nW/K, and the e-ph coupling constant $\Sigma = 1.5 \times 10^8$ WK^{-5}m^{-3}. The exponent $n = 5$ in the power law is the characteristic of the e-ph coupling. We performed the same analysis for all the bare Ir/Pt TESs and the fitted thermal parameters are summarized in Table 1.

We also performed alternative fits to the P-T data with n as a free parameter in Eq. (1). The orange dash-dotted line in Fig. 3(b) shows the example for MCC-4-3 which resulted

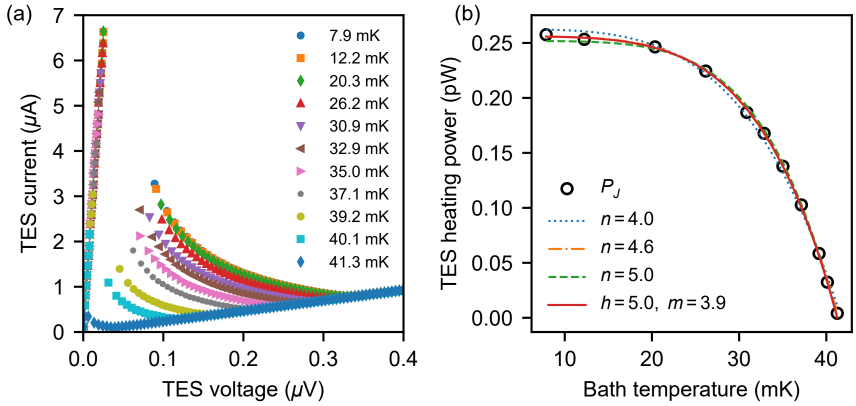

Fig. 3: (a) Measured TES current vs. TES bias voltage for MCC-4-3 at a variety of bath temperatures. The ~ 4 mΩ parasitic resistance is not subtracted from the IV curves so the superconducting region in the vicinity of zero bias is not vertical. (b) Measured TES Joule power vs. bath temperature for the same TES and the power law fits. The orange dash-dotted line and the green dashed line are the fits to Eq. (1) with n floating and $n = 5$, respectively. The fitted parameters for $n = 5$ fit are listed in Table 1. The red solid line is the two-block fit with $h = 5$ fixed. The blue dotted line is the one-block fit with $n = 4.0$ fixed to show degradation of the fit when n deviates from e-ph coupling.

$n = 4.6$. For these fits, the fitted exponent n spreads from 4.3 to 5.3. The induced changes of T_c's and G's from the $n = 5$ fits are not significant, however, the spread of Σ is much larger since it strongly depends on n. We therefore standardized all the fits in Table 1 by fixing $n = 5$ so the fitted parameters are in a more accessible form, without losing fidelity in predicting the TES properties. To better understand the deviation of n from the characteristic value 5, for the worst case $n = 4.3$ with IrPt-S005 in the $n < 5$ fits, we conducted the two-block fit with $h = 5$. This time we obtained $m = 3.9$ and $\Sigma = 2.2 \times 10^8$ WK^{-5}m^{-3}. The second weak thermal link may be attributed to the Kapitza resistance between the TES phonons and the thermal bath. The value of Σ is slightly enhanced, by 5%, and is consistent with the dominant thermal conductance being e-ph coupling in the TES even in the presence of this second weak thermal link. The deviations for the $n > 5$ fits are not yet fully understood, but they are still in the regime of e-ph coupling. One possible scenario is that disorders in the TESs weaken the e-ph coupling [5], which up shifts n, and Σ's for these fits will also be up shifted as a result. These alternative fits, both for the $n < 5$ and $n > 5$ cases, are consistent with the dominant cooling mechanism for the TESs being e-ph coupling.

The spread of Σ for the Ir/Pt bilayers in Table 1 is also correlated with the T_c variations within the same batch of devices, MCC-4-x and MC-12-x, each deposited with the same process. The T_c variations are independently confirmed by the RT measurements. These variations may come from the nonuniformity of the deposition process, which will need further investigation.

Table 2: Configurations for TESs with Au pads. The TES-Au interface structure is depicted in Fig. 5(a). P_{sat} is the Joule power measured at the base temperature below 7 mK. T_c and G are from the *single-block* power-law fits to Eq. (1) with *n floating*, neither of which is sensitive to the value of n around the best fit.

Device	Pt (nm)	TES (μm)	Au pad (μm $\times$ μm)	TES-Au $x/y/z$ (μm)	T_c (mK)	P_{sat} (pW)	G (nW/K)
MC-12-2	50	300	300 × 300	5/10/5	54.6	34.2	3.3
MC-12-4	50	300	900 × 900	5/10/5	55.0	173.2	16.2
MCC-4-8	60	300	230 × 300	5/10/5	42.5	10.7	1.3
MCC-4-10	60	300	900 × 300	5/10/5	39.6	22.1	2.8
MCC-4-11	60	300	900 × 300	5/10/10	41.2	29.4	3.6
MCC-4-12	60	300	900 × 300	5/5/5	42.0	32.3	3.9

4.3 Σ for Au

To measure the e-ph coupling constant Σ for Au, we have fabricated two batches of TES devices with Au pads, MC-12-x and MCC-4-x. Table 2 lists the detailed parameters of these devices. Both batches have 300 μm square Ir/Pt bilayer TES with 100 nm thick Ir. The Pt layer thicknesses are 50 nm and 60 nm, giving the measured T_c's around 55 mK and 40 mK for MC-12-x and MCC-4-x, respectively. The Au pad size is varied within each batch while keeping the TES-Au interface unchanged. The TES-Au interface variation is introduced within the batch MCC-4-x while keeping the Au pad size constant. We were able to study the dependence of TES thermal properties on both the Au volume and TES-Au interface with the two batch of devices.

4.3.1 Existence of a second weak thermal link

By taking the IV curves and fitting the P-T data for the TESs with Au pads, the e-ph coupling constant Σ for Au could be extracted similarly as that for the Ir/Pt bilayers discussed in Sec. 4.2. But there are new challenges to the data analysis brought in by the addition of the Au pads, which introduces additional complexity to the devices. Fig. 4(a) shows the measured P-T curves for MC-12-4 in black squares and MC-12-2 in black circles. The single-block fits to Eq. (1) for the two devices are shown as the solid black line with fitted $n = 5.2$ and the dash-dotted blue line with fitted $n = 5.3$, respectively. The single-block model appears to be a rather good description to these devices, and the values of the fitted exponent n indicate that the dominant heat conduction is through e-ph coupling. However, as shown in Fig. 4(b), the saturation power of the TESs with Au pads does not scale proportionally to the volume of the Au pads, which is expected for e-ph coupling. The saturation behavior suggests that there exists a second weak thermal link in these devices besides the e-ph thermal conductance of the Au pads. Consequently, the e-ph coupling constant Σ for Au cannot be extracted from the single-block fits in the same way as that for the bare Ir/Pt TESs. Nonetheless, the transition temperature T_c and the total thermal conductance G of the device are nearly model independent and, as such, their values from the single-block fits with a *floating n* are listed in Table 2, as well as the measured TES saturation powers.

With the addition of Au pads to the Ir/Pt TES, the dominant thermal conductance of the device is through the Au pads. The saturation power of the 300 μm square bare Ir/Pt TES is less than 5% of that for the TES with the smallest Au pads for both batches. This indicates that the weak thermal link that throttles the e-ph thermal conductance of the Au pads resides either between the Au pads and the thermal bath or between the Ir/Pt bilayer and the Au

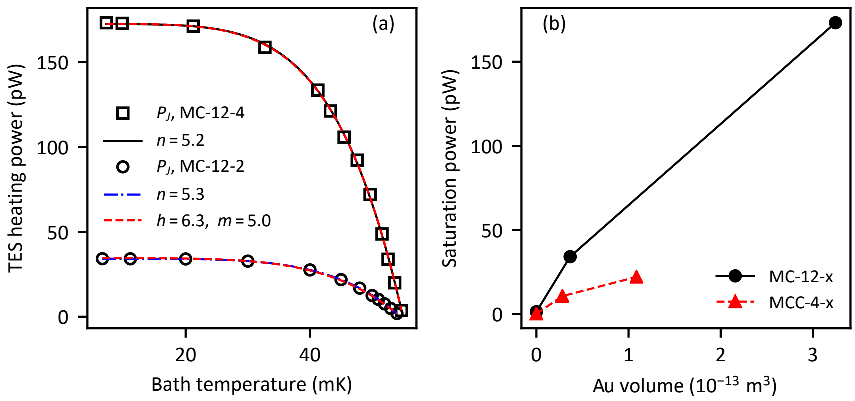

Fig. 4: (a) P-T data for MC-12-4 and Mc-12-2 and various fits. (b) TES saturation power for TESs with Au pads vs. Au volume for two batches of devices, MC-12-x in black dots and MCC-4-x in red triangles. The two points near the origin are the bare Ir/Pt TESs. The sub-linear dependence of the P-V curves indicates that there is a second weak thermal link in these TESs.

pads. For the former case, the coupling between the Au pad phonons and the thermal bath would reduce the exponent n from the single-block fits to less than 5, as we have observed for the bare Ir/Pt TESs. This contradicts the single-block fitting results for the TESs with Au pads, where the fitted n's are between 4.8 and 5.3, and the TESs with larger Au pads tend to favor larger n's. So this leads to the conclusion that the second weak thermal link is between the electrons of the Ir/Pt TES and the Au pads.

We thus varied the TES-Au interface to investigate its influence on the TES thermal conductance. TESs MCC-4-10, -11, and -12 with TES-Au interfaces 5/10/5, 5/10/10, and 5/5/5, respectively, in the notion of Fig. 5(a) and Table 2, were fabricated to test the interface effects on the total thermal conductance. These devices all have relatively large, 900 μm $\times$ 300 μm, Au pads intended to saturate the second weak thermal link. We indeed observed thermal conductance changes due to the TES-Au interface variation. From the interface 5/10/5 to 5/10/10, the Au-Ir/Pt overlap on the inner side of the Nb leads is increased by 5 μm, and the saturation power of the device goes up from 22 pW to 29 pW. Similarly, there is a 10 pW TES saturation power increase from the 5/10/5 to the 5/5/5 interface. These results clearly show that the second weak thermal link is at the TES-Au interface, and both decreasing the width of the Nb leads and increasing the overlap between Au and the Ir/Pt TES can increase the interface thermal conductance.

4.3.2 Σ_{Au} and G_{xyz} near transition

With the thermal conductance of the TES-Au interface properly accounted for, Σ_{Au} can be derived from the TES thermal conductance near transition, assuming the nature of the Au thermal conductance is known. Fig. 2(b) shows the thermal circuit for the TESs with Au pads, depicting the second weak thermal link between the electrons of the Ir/Pt TES and the Au pads. The dashed line between the TES electrons and the thermal bath means the direct thermal conductance, G_{TES}, between them is generally negligible. At bath temperatures close to the transition temperature, by Fig. 2(b) and Eq. (10), the total thermal conductance

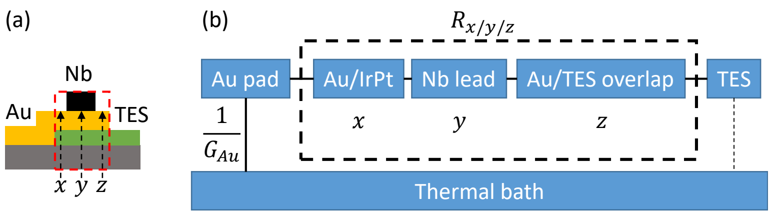

Fig. 5: (a) Cross section view of the TES-Au interface. x, y, and z are the widths in μm of the three overlap regions Au over Ir/Pt outside Nb leads, Nb over Au and Ir/Pt, and Au over Ir/Pt inside Nb leads, respectively. (b) Schematic of the thermal impedances for the TESs with Au pads and the TES-Au interface. The dashed line between TES and thermal bath means the direct thermal conductance between the Ir/Pt TES and the thermal bath is generally negligible.

of the device is

$$G = G_{\mathrm{TES}} + \frac{1}{1/G_{xyz} + 1/G_{\mathrm{Au}}}, \tag{11}$$

where G_{xyz} is the TES-Au interface thermal conductance and $G_{\mathrm{Au}} = 5\Sigma_{\mathrm{Au}}\Omega_{\mathrm{Au}}T^4$ is the thermal conductance for Au, assumed due to e-ph coupling based on the single-block fits. Here we have kept the term G_{TES} for the completeness of formality, although its effect on the numerical results is insignificant. G_{xyz} and Σ_{Au} can be solved for from Eq. (11) for a complete set of TESs.

Consider the set MC-12-1, -2, and -4, for which G_{TES} is 0.12 nW/K from the measurement of MC-12-1, and the rest pair MC-12-2 and -4 share two common unknowns G_{xyz} and Σ_{Au} since they both have the same 5/10/5 TES-Au interface and the same film deposition process. The temperature dependence of G_{xyz} is neglected because the T_c difference is small. The effect on Σ_{Au} from a temperature gradient in the Au pads is less than 8% for the largest pad size from our estimates based on the measured electrical resistivity of a reference device. So we assumed the same batch of devices share the same value of Σ_{Au} considering the fact that the model uncertainty dominates the measurement. With the measured total thermal conductances for MC-12-2 and -4, we obtained $G_{xyz} = 32.0$ nW/K and $\Sigma_{\mathrm{Au}} = 2.2 \times 10^9$ WK^{-5}m^{-3} by solving Eq. (11). More details are listed in Table 3. We can see that for MC-12-4, the thermal conductance of Au is starting to surpass that for the TES-Au interface. Σ_{Au} for this device extracted from the single-block fit would be significantly underestimated. The results for the pair MCC-4-8 and -10 following the same method are also listed in Table 3, which are $G_{xyz} = 7.4$ nW/K and $\Sigma_{\mathrm{Au}} = 3.2 \times 10^9$ WK^{-5}m^{-3}. The same Σ_{Au} value was then applied to MCC-4-11 and -12, which gave $G_{xyz} = 12.4$ nW/K and $G_{xyz} = 13.2$ nW/K, respectively. For devices MCC-4-x with Au pads, G_{xyz} is always much larger than G_{Au}.

4.3.3 Σ_{Au} and G_{xyz} from two-block fits

In Sec. 4.3.2, we have calculated the TES-Au interface thermal conductance G_{xyz} and the e-ph coupling constant Σ_{Au} for the devices in Table 3, with the assumption that the thermal conductance of Au is due to e-ph coupling. In this section, we apply the two-block fitting method described in Sec. 4.1 directly to the P-T data of the same devices without assuming

Table 3: Thermal conductances near TES transition temperature calculated from the *two-block* formula given in Eq. (11), and the derived e-ph coupling constant for Au assuming $G_{\mathrm{Au}} = 5\Sigma_{\mathrm{Au}}\Omega T^4$. G, G_{xyz}, G_{Au}, and G_{TES} are total, TES-Au interface, Au pad, and Ir/Pt TES thermal conductances, respectively.

Device	G (nW/K)	G_{xyz} (nW/K)	G_{Au} (nW/K)	G_{TES} (nW/K)	Σ_{Au} (WK^{-5}m^{-3})
MC-12-2	3.3	32.0	3.5	0.12	2.2×10^9
MC-12-4	16.2	32.0	32.2	0.12	2.2×10^9
MCC-4-8	1.3	7.4	1.5	0.03	3.2×10^9
MCC-4-10	2.8	7.4	4.3	0.03	3.2×10^9
MCC-4-11	3.6	12.4	5.0	0.03	3.2×10^9
MCC-4-12	3.9	13.2	5.4	0.03	3.2×10^9

Table 4: *Two-block* fitting results of P-T data according to Eq. (3). G, G_{xyz}, and G_{Au} are the total, TES-Au interface, and Au pad thermal conductances, respectively. h and m are the power-law exponents for the TES-Au interface and Au pads, respectively. Σ_{Au} is calculated with $G_{\mathrm{Au}} = m\Sigma_{\mathrm{Au}}\Omega T^{m-1}$.

Device	G (nW/K)	G_{xyz} (nW/K)	G_{Au} (nW/K)	h	m	Σ_{Au} (WK^{-5}m^{-3})
MC-12-2	3.2	32.1	3.5	6.3	5.0	2.2×10^9
MC-12-4	16.4	33.3	32.1	6.3	5.0	2.2×10^9
MCC-4-8	1.3	7.4	1.5	1.8	5.0	3.1×10^9
MCC-4-10	2.7	7.0	4.5	1.8	5.0	3.1×10^9
MCC-4-11	3.6	13.7	4.9	5.0	5.0	3.1×10^9
MCC-4-12	3.9	14.5	5.3	4.2	5.0	3.1×10^9

the nature of Au thermal conductance. We first fitted the pairs MC-12-(2,4) and MCC-4-(8,10). Each pair shared a common set of fitting parameters, K_1, h, Σ_{Au}, and m, because they are described by the same thermal circuit in Fig. 2(b) but with different Au pad size. The T_c's of a pair were fixed at their individual single-block fitted values listed in Table 2. The contributions of G_{TES} were neglected in the two-block fits for simplicity. The fitted curves for the pair MC-12-(2,4) are shown in Fig. 4(a) as the dashed red lines with fitted $h = 6.3$ and $m = 5.0$. The detailed fitting results for both pairs are listed in Table 4. The fitted values of $m = 5.0$ for both pairs, MC-12-(2,4) and MCC-4-(8,10), are consistent with the assumption that the thermal conductance of Au is through e-ph coupling. The derived thermal parameters G, G_{xyz}, G_{Au}, and Σ_{Au} are in good agreement with those in Table 3. G_{xyz} for MCC-4-10 is dragged slightly lower because it has a lower T_c than MCC-4-8. The two-block fits for MCC-4-11 and -12 were conducted individually each with T_c, Σ_{Au}, and m fixed. The adopted G_{Au} in the fits are slight lower than those in Table 3, which pushed the fitted G_{xyz} slightly higher.

4.4 TES-Au interface thermal conductance

Our LDs require a subdominant TES-Au interface thermal conductance around 10 nW/K or higher. From Tables 3 and 2, we can see that, by changing the interface from 5/10/5 to either 5/10/10 or 5/5/5, i.e., by either increasing the TES/Au overlap or reducing the Nb lead width, this goal is already met at 40 mK. And there is still room for further improvement. More information about G_{xyz} can in principle be extracted from the two-block fits, where the exponent h gives its temperature dependence. However, since G_{Au} almost universally dominates for the devices we measured, it is expected that the model uncertainty on G_{xyz} will be large. Compared to MC-12-x, the constraining power to G_{xyz} from MCC-4-x is substantially weaker because of stronger dominance of G_{Au}, and therefore the best-fit values of m are subject to larger uncertainties.

5 Conclusions

We have measured the thermal conductances of the Ir/Pt bilayer, Au pad, and TES-Au interface for Ir/Pt TESs with and without Au pads. For both types of devices, we found that there was a second weak thermal link present besides the one due to e-ph coupling in Ir/Pt bilayer or Au. This necessitated two-thermal-block models to fit the P-T data to decouple the effect of the second weak link. For bare Ir/Pt TESs, the second weak thermal link was between the TES phonons and the thermal bath, possibly due to the Kapitza impedance between the Ir/Pt bilayer and the Si substrate; the dominant thermal impedance was still e-ph coupling despite its presence. Whereas for TESs with Au pads, the addition of Au pads increased the total thermal conductance of the device significantly, meanwhile, the second weak link emerged at the interface between the Ir/Pt bilayer TES and the Au pads. By varying the designs of the TES-Au interface, we found that both reducing the Nb lead width and increasing the TES/Au overlap within the TES current path could increase the interface thermal conductance. The measured values of the TES-Au interface thermal conductance with improved designs already meet the requirement of our LD, and there is still room for further improvement.

The e-ph coupling constants for Ir/Pt bilayers and Au are extracted from the P-T measurements. The average Σ for Ir/Pt bilayer in the T_c range between 32 mK and 70 mK is 1.9×10^8 WK^{-5}m^{-3} with 1.2×10^8 WK^{-5}m^{-3} the lowest and 2.7×10^8 WK^{-5}m^{-3} the highest. Σ's for Au are 2.2×10^9 WK^{-5}m^{-3} at 40 mK and 3.2×10^9 WK^{-5}m^{-3} at 55 mK. The values for Au are consistent with earlier measurements [7, 8, 9, 10, 11]. The spread of Σ either for Ir/Pt or Au is likely dominated by the uncertainties of the physics model , i.e., there are mechanisms that contribute to the measured thermal conductance not captured by the power law for e-ph coupling. The uncertainties in temperature and voltage measurements as well as film thicknesses are too small to account for the observed spread.

The datasets generated during and/or analysed during the current study are available from the corresponding author on reasonable request.

Acknowledgements This work was supported by the US Department of Energy (DOE), Office of Science under Contract No. DE-AC02-05CH11231 and DE-AC02-06CH11357, and by the DOE Office of Science, Office of Nuclear Physics under Contract No. DE-FG02-00ER41138. Superconducting thin films synthesis was supported by the DOE Office of Science, Office of Basic Energy Sciences, Materials Sciences and Engineering Division. Use of the Center for Nanoscale Materials, an Office of Science user facility, was supported by the DOE Office of Science, Office of Basic Energy Sciences under Contract No. DE-AC02-06CH11357.

References

1. T.C.I. Group. Cupid pre-cdr (2019). URL `https://arxiv.org/abs/1907.09376`
2. K. Irwin, G. Hilton, *Transition-Edge Sensors* (Springer Berlin Heidelberg, Berlin, Heidelberg, 2005), pp. 63–150. DOI 10.1007/10933596_3. URL `https://doi.org/10.1007/10933596_3`

3. R. Hennings-Yeomans, C.L. Chang, J. Ding, A. Drobizhev, B.K. Fujikawa, S. Han, G. Karapetrov, Y.G. Kolomensky, V. Novosad, T. O'Donnell, J.L. Ouellet, J. Pearson, T. Polakovic, D. Reggio, B. Schmidt, B. Sheff, V. Singh, R.J. Smith, G. Wang, B. Welliver, V.G. Yefremenko, J. Zhang, J. Appl. Phys. **128**(15), 154501 (2020). DOI 10.1063/5.0018564. URL `https://doi.org/10.1063/5.0018564`
4. V.F. Gantmakher, Rep. Progr. Phys. **37**(3), 317 (1974). DOI 10.1088/0034-4885/37/3/001
5. J.T. Karvonen, L.J. Taskinen, I.J. Maasilta, Phys. Rev. B **72**, 012302 (2005). DOI 10.1103/PhysRevB.72.012302. URL `https://link.aps.org/doi/10.1103/PhysRevB.72.012302`
6. J.N. Ullom, D.A. Bennett, Superconductor Science Technology **28**(8), 084003 (2015). DOI 10.1088/0953-2048/28/8/084003
7. M.L. Roukes, M.R. Freeman, R.S. Germain, R.C. Richardson, M.B. Ketchen, Phys. Rev. Lett. **55**, 422 (1985). DOI 10.1103/PhysRevLett.55.422. URL `https://link.aps.org/doi/10.1103/PhysRevLett.55.422`
8. M. Nahum, J.M. Martinis, Applied Physics Letters **63**(22), 3075 (1993). DOI 10.1063/1.110237. URL `https://doi.org/10.1063/1.110237`
9. F.C. Wellstood, C. Urbina, J. Clarke, Phys. Rev. B **49**, 5942 (1994). DOI 10.1103/PhysRevB.49.5942. URL `https://link.aps.org/doi/10.1103/PhysRevB.49.5942`
10. C.S. Yung, D.R. Schmidt, A.N. Cleland, Applied Physics Letters **81**(1), 31 (2002). DOI 10.1063/1.1491300. URL `https://doi.org/10.1063/1.1491300`
11. D.R. Schmidt, C.S. Yung, A.N. Cleland, Phys. Rev. B **69**, 140301 (2004). DOI 10.1103/PhysRevB.69.140301. URL `https://link.aps.org/doi/10.1103/PhysRevB.69.140301`